Supplementary Information

Supplementary Figures

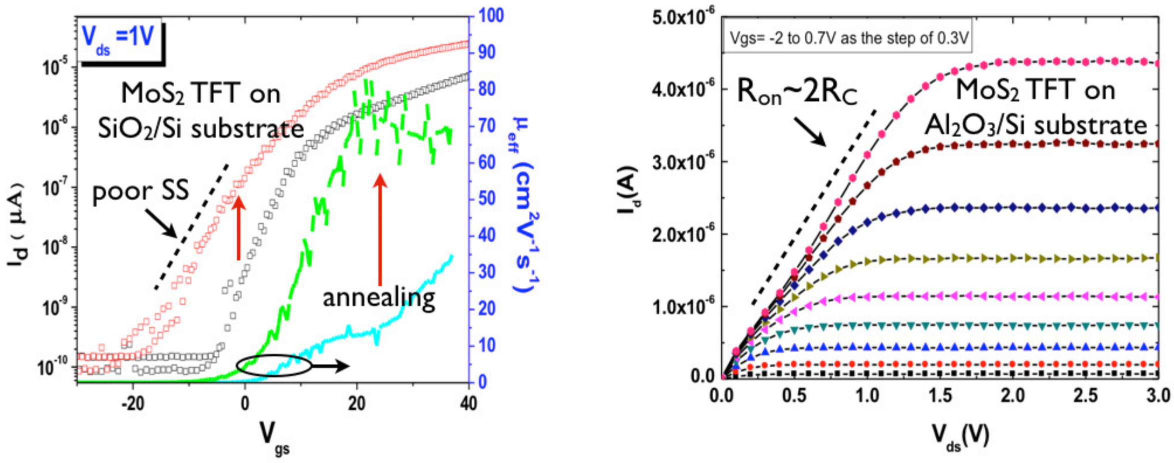

Supplementary Fig S1: Multilayer MoS_2 FETs on SiO2/Si substrates, and contact resistance effects. (Left): Transfer curves and effective mobility of multilayer MoS_2 TFTs fabricated on SiO_2/Si substrates showing poor switching characteristics. The performance improves marginally upon annealing. (Right): Estimation of the contact resistance from the on-resistance of a multilayer MoS_2 TFT on ALD Al_2O_3/Si substrate.

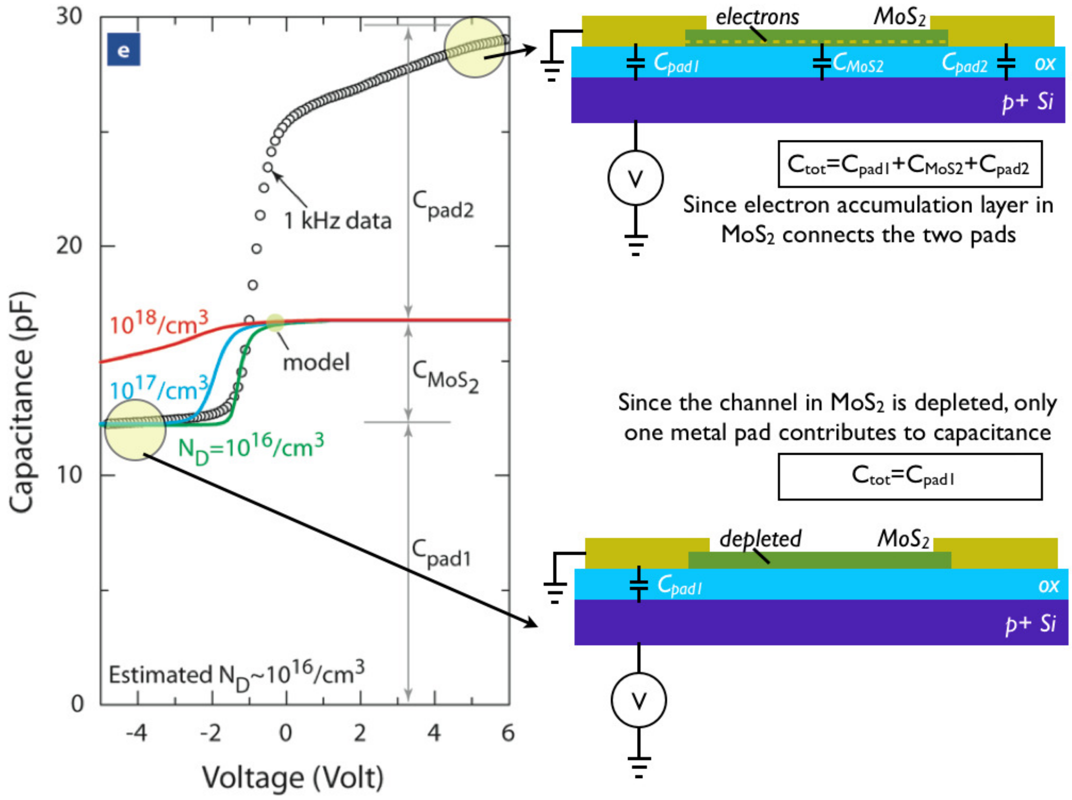

Supplementary Fig S2: Capacitance-voltage curves of MoS_2 TFT devices. The floor or 'off-state' capacitance corresponds to the pad capacitance of a single pad, whereas the on-state capacitance corresponds to that of the MoS_2 layer *and* two ohmic pads.

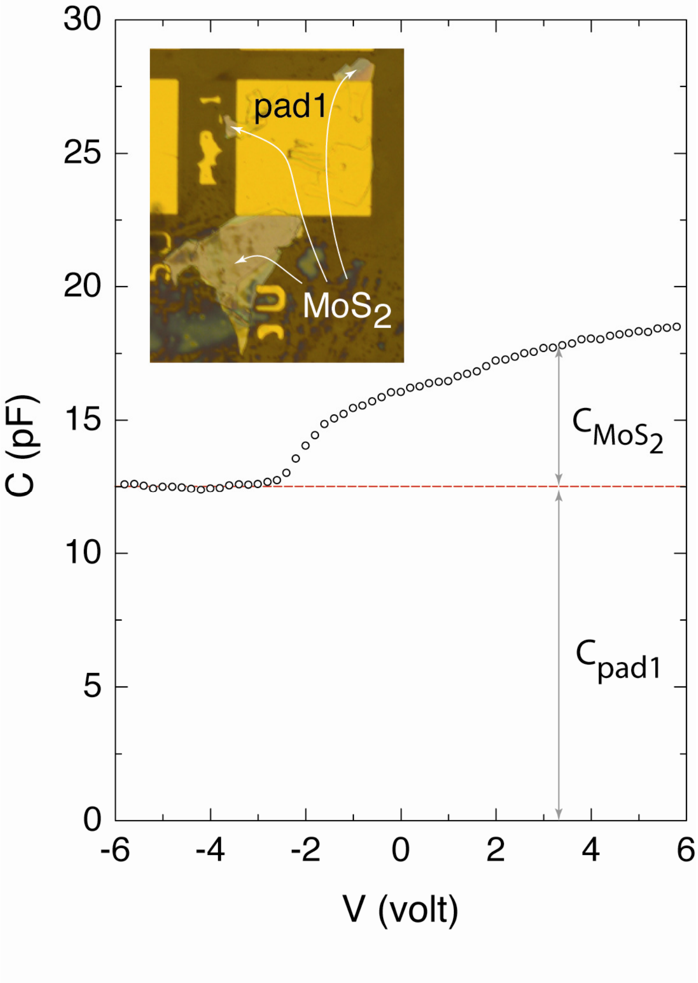

Supplementary Fig S3: Capacitance-voltage curves of a single MoS_2 flake connected to a metal pad. The floor or 'off-state' capacitance corresponds to the pad capacitance of a single pad, similar to Fig S2, whereas the on-state capacitance for this case corresponds to that of the MoS_2 flake. Note that it is necessary to locate a large flake for such a measurement to be successful.

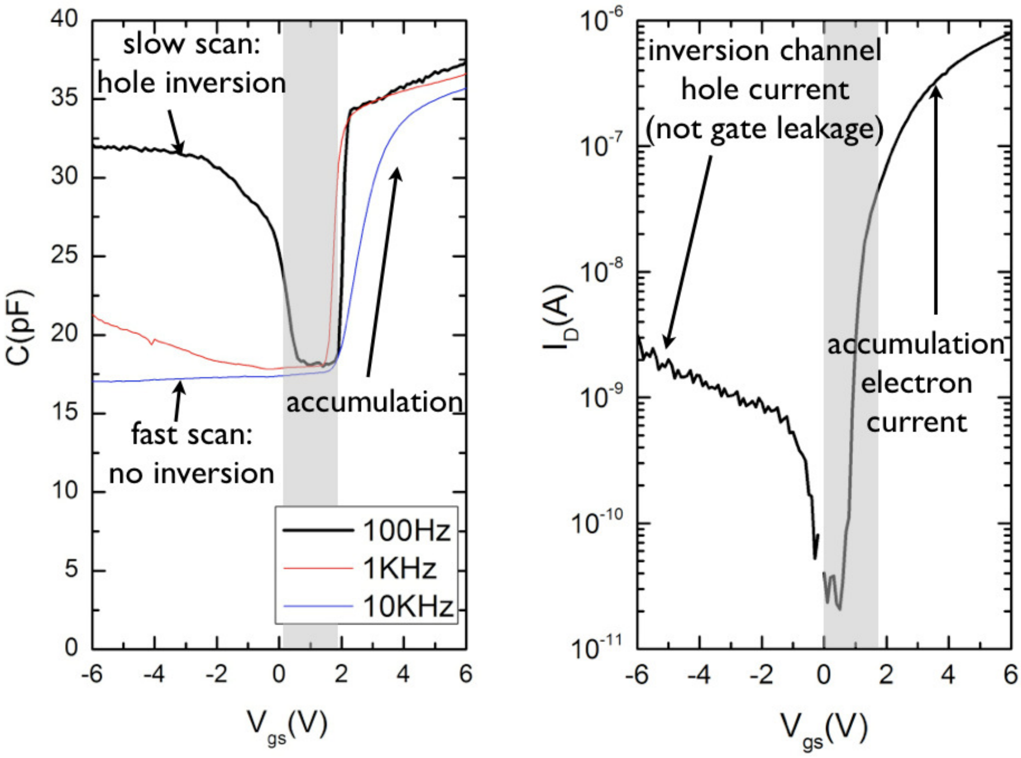

Supplementary Fig S4: Capacitance-voltage measurement of multilayer MoS_2 TFTs and corresponding drain currents. The low-frequency scans clearly indicate the formation of an inversion layer of holes. Since the ohmic contacts are formed to the electron channel, the slow RC charging from the Schottky barrier contacts to the hole gas results in the delay in hole channel formation. With the optimal contacts, inversion hole channels are expected to form with equal ease as the n-channel accumulation layers.

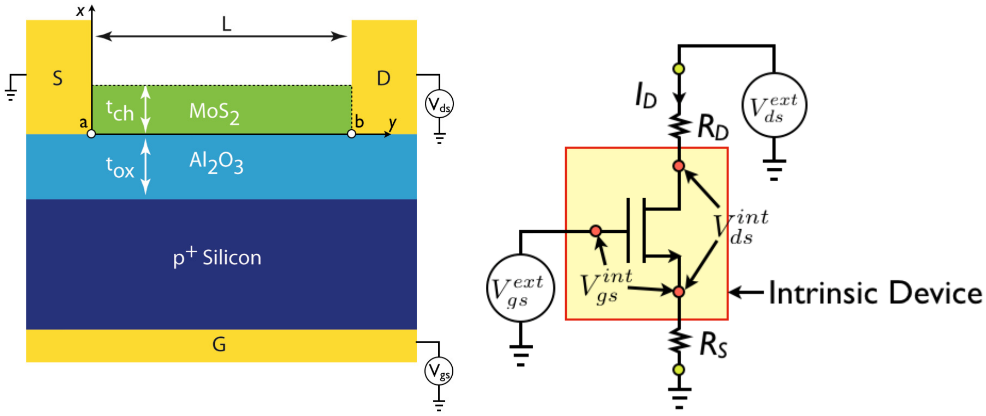

Supplementary Fig S5: Device geometry of the multilayer MoS_2 TFT and the circuit diagram showing the effect of extrinsic contact resistances on measured gate and drain voltages compared to the intrinsic transistor.

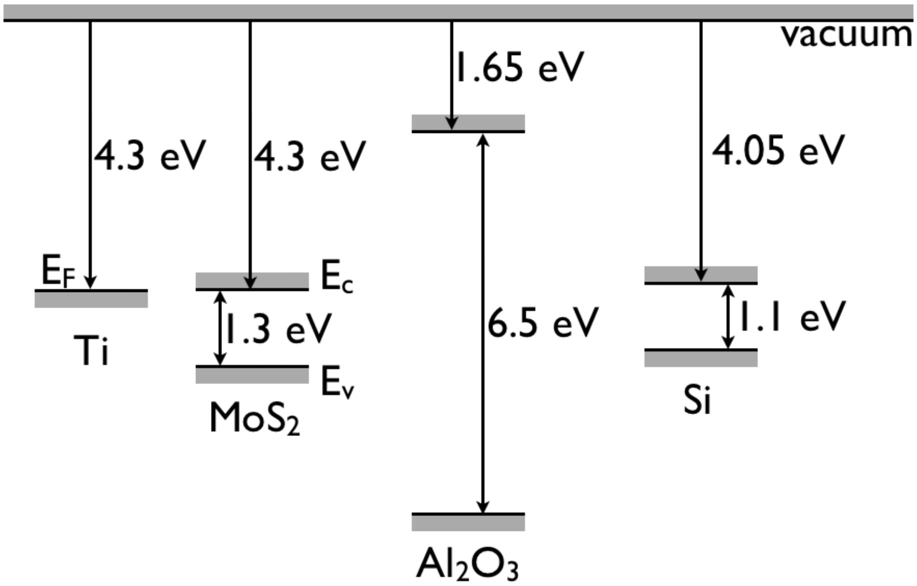

Supplementary Fig S6: Work function of Ti, and electron affinities and bandgaps of silicon, ALD Al_2O_3, and multilayer MoS_2 used for the energy band-diagram calculations. The band offsets can be directly inferred. The band alignment shows the feasibility of Ti for ohmic contact to the conduction band of MoS_2.

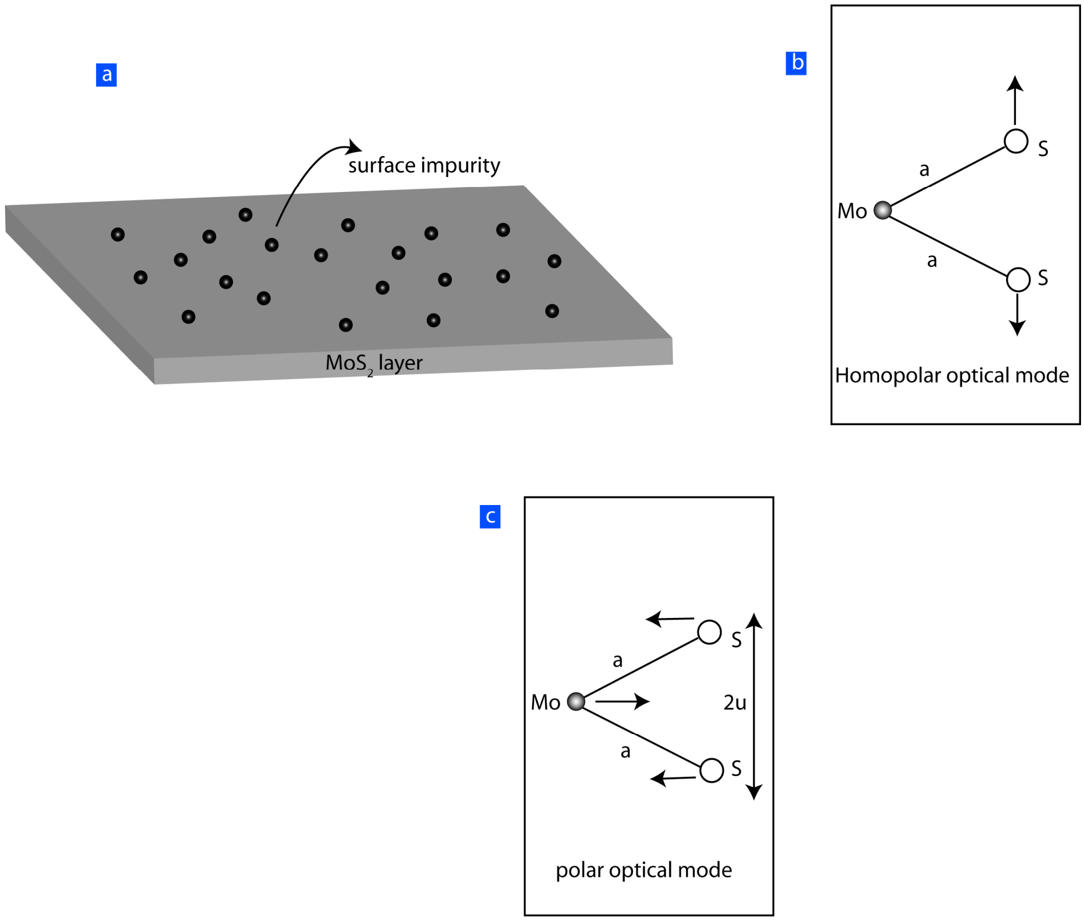

Supplementary Fig S7: Impurities and phonon modes in MoS_2 that affect charge transport. (a) Ionized impurities at the surface of a MoS_2 layer. Relative movements of molybdenum and sulphur atoms for (b) homopolar phonon mode, (c) polar optical phonon mode. Note that in homopolar modes, the sulfur atoms move out-of-plane in opposite directions.

Supplementary Methods

Device Characteristics and Modeling

a) Device Characteristics: The initial multilayer MoS_2 TFTs fabricated on 300nm SiO_2/Si substrates looked similar to earlier reports, exhibiting poor subthreshold characteristics as shown in Supplementary Fig S1. Annealing of these transistors improved the mobility and the current drive. Since the subthreshold slope is given by $SS = (1 + \frac{C_S + C_{it}}{C_{ox}})\frac{kT}{q}\ln 10$, the oxide capacitance $C_{ox} = \varepsilon_{ox} / t_{ox}$ is 20 times smaller for TFTs on SiO_2/Si compared to Al_2O_3/Si. This explains the high SS for the initial TFTs, compared to the near-ideal values for those on ALD high-*k* substrates, as discussed in the main text. The annealing strategy was used for all subsequent devices.

The contact resistance in traditional FETs is extracted from transmission-line method (TLM) measurements. However, due to the small area of the currently available multilayer MoS_2 flakes, such a measurement was not possible using optical lithography. Another dependable method for the extraction of the contact resistance is by measuring the on-resistance of the FET at a very large gate bias. The channel is highly conductive under this condition, and the current in the linear region flowing in the channel is limited by the source and drain contact resistances connected in series to the drain voltage source. The I_D-V_{DS} curves merge for various gate biases when this condition is achieved, since the gate capacitor cannot control the contact resistance. This feature is shown for a TFT in Supplementary Fig S1 (right), from where a R_C~17 kΩ is extracted. The contact resistance varied between devices close to this value, and respective values were used for subsequent simulations. For applications of multilayer MoS_2 for TFTs, lowering of the contact resistance will lead to increase in drive currents.

b) Capacitance-Voltage measurements & Inversion channel formation: Supplementary Fig S2 is necessary to explain the measured C-V profiles under various bias conditions. The measured capacitance floor (~12 pF) corresponds accurately to the net capacitance of one ohmic metal pad with the back gate. However, when an accumulation layer of electrons is formed in the MoS_2 layer, it connects the two pads electrically. Since there is no current flow between them, the two pads and the MoS_2 accumulation layer are equipotential – they are all grounded. This explains the measured capacitance behavior. To further confirm this interpretation, we were able to locate a large MoS_2 flake that was in contact with just one metal pad: the measured C-V curve is shown in Supplementary Fig S3, and confirms our interpretation. Note that the pad capacitance floor is 12 pF in both Supplementary Figs S2 and S3. The net capacitance of the MoS_2 is now directly evident in Supplementary Fig S3. We note however, that this is a different (and much larger and of a different thickness) flake than those for which the FETs were measured. Therefore, a direct comparison of the model is not warranted.

In addition, some (not all) C-V measurements indicated a recovery of the capacitance at large negative voltages, indicating the formation of an inversion layer of holes in the MoS_2 layer. However, this requires efficient ohmic contacts to the valence band, which was not intended in the experiment. It is also indicated in Fig 2(b) in the TFT transfer curves. This preliminary observation is of immense interest given the possibility of complementary logic devices. We discuss this further to the extent we have been able to investigate it till now. As alluded to in the main text and in Fig 2(b) there, some devices showed the formation of an inversion channel of holes at large negative gate biases. This is expected of a semiconductor layer, as long as the contacts are able to electrically connect to the valence band of the semiconductor. Though the contacts are designed for the conduction band electrons, the high contact resistance indicates that it is not yet ideal. Thus, one can expect a Schottky-barrier contact to be formed to the valence band. If so, it should be possible to observe conduction by inversion channels in the multilayer MoS_2 TFTs. A fingerprint of an inversion channel is through capacitance-voltage measurements that are complementary to the current-voltage measurements. For devices that show inversion channel current conduction, we performed capacitance-voltage scans, and indeed observed the recovery of the capacitance only when the scans were performed at a slow rate. The complementary C-V and I-V curves are shown in Supplementary Fig S4 for a device that did show the presence of an inversion channel.

As is evident in the figure, the capacitance at large negative bias voltages is able to recover under slow scan, but not under rapid scans. This is completely identical to what happens in a silicon MOS structure[28]. Since the contact is electron-rich, and there is no direct source of holes, they have to form by thermal interband excitations or by the minute leakage currents into the contacts. This is a slow process, requiring ~ms to ~second time scales, depending on the size of the bandgap and the nature of the contacts. It is foreseen that with proper choice of metal workfunctions, this preliminary observation will seed the realization of complementary n-FET and p-FET based multilayer MoS_2 TFTs, with significant technological impact.

c) Modeling of device characteristics: The electrical characteristics of the back-gated FET structure are modeled using a long-channel model. The device geometry is shown in Supplementary Figure S5. The transistor model uses the fact that under flat-band conditions, the carrier density at all points (x, y) in the MoS$_2$ channel is equal to the unintentional doping, i.e., $n_{FB}(x, y) = N_D$. When the potential in the channel is changes due to gate and drain voltages, the electron density changes to $n(x, y) = N_D \exp[\beta V(x, y)]$, where $V(x, y) = \psi(x) - V_{ch}(y)$ is the long-channel approximation and $\beta = q / kT$ is the inverse of the thermal voltage. The Poisson equation in the channel is given by $\partial^2\psi / \partial x^2 \approx -(qN_D / \varepsilon_s)[1 - \exp[\beta(\psi - V_{ch}]]$in the gradual channel approximation. This equation has no analytic solutions, but for bias conditions for which the device is "on", the exponential term dominates, and the equation can be integrated to yield the solutions for the potential ψ as a function of the drain-induced potential V_{ch}. The solution is $\psi = V_{GF} + (2/\beta)\cdot W[\exp[\beta(V_{GF} + V_{ch})/2] \times C_D / C_{ox}]$, where $V_{GF} = V_G - V_{FB}$, $C_D = \varepsilon_s / L_D\sqrt{2}$ is the accumulation or 'Debye' capacitance with $L_D = \sqrt{\varepsilon kT / q^2 N_D}$ as the Debye length in MoS$_2$, and $W(...)$ is the Lambert-W function, the solution of the equation $W(u)\cdot\exp[W(u)] = u$. Since the source and the drain points labeled 'a' and 'b' in Supplementary Fig S5 have $V_{ch} = 0$ and $V_{ch} = V_{ds}$ respectively, the values ψ_a and ψ_b are obtained as a function of the gate and the drain bias voltages. The drain current is then obtained by integrating the transport equation in the long channel approximation. Doing so, one obtains[29]

$$I_D = \frac{W}{L}\mu_{eff}C_{ox}[(V_G + \frac{2}{\beta})(\psi_b - \psi_a) - \frac{1}{2}(\psi_b^2 - \psi_a^2)] + \frac{W}{L}\frac{q}{\beta}\mu_{eff}n_i t_{ch}(1 - \exp[-\beta V_{ds}]), \qquad \text{(S1)}$$

where n_i is the intrinsic carrier concentration in MoS_2 due to thermal interband excitation, and μ_{eff} is the effective (x-averaged) electron mobility. We have used this formalism to model the current-voltage curves as shown in Figure 2 of the main text. However, the measured gate and drain voltages are not those of the intrinsic device, but are higher due to potential drops at the source and drain contact resistances, as shown in Supplementary Fig S4. The extrinsic voltages are given by $V_{gs}^{ext} = V_{gs}^{\text{int}} + I_D R_S$ and $V_{ds}^{ext} = V_{ds}^{\text{int}} + I_D (R_S + R_D)$. We use $R_S = R_D = R_C$, the contact resistance for the evaluation. The value of R_C is easily obtained at a high gate bias, since under that condition the channel resistance is negligible, and the net resistance is $V_{ds} / I_D = 2R_C$. We measure $R_C \sim 20\ \text{k}\Omega$ for the device modeled. The values are expected to reduce with further process development. The fit to the experimental data in Fig 2(d) of the main text requires an effective mobility of 100 $\text{cm}^2/\text{V}\cdot\text{s}$. The fitting can be considered to be an effective extraction of the mobility, which is complemented by calculation of the mobility due to various scattering mechanisms as described later in this supplementary section.

d) Energy band diagram simulation details: The energy band diagrams to explain the device characteristics were calculated by solving Poisson equation and Schrödinger equation self-consistently. The Schrödinger equation is solved in the effective mass approximation using a freely available tool[30] by incorporating material properties specific to the device. The energy band offsets and energy bandgaps used in the calculation for silicon, ALD Al_2O_3, and multilayer MoS_2 are shown in Supplementary Fig S6. The values for MoS_2 were taken from Refs[31, 32]. The required material parameters for the simulations are shown in Supplementary Table ST1.

Modeling of Charge Transport

Since the MoS_2 TFTs studied here are long channel (L~10 μm) devices, carrier transport phenomena are best explained in the drift-diffusion scheme. The electrical response is linear and the change in the carrier distribution function and the resulting conductivity depends linearly on the electric field[33]. In such a scenario, the temperature-dependent carrier mobility is given by

$$\mu(T) = \frac{e}{m^*}\left[\frac{\int \tau(\varepsilon)\varepsilon e^{-\varepsilon/k_B T}\,d\varepsilon}{\left(k_B T\right)^2}\right], \qquad \text{(S2)}$$

where $\tau(\varepsilon)$ is the energy-dependent momentum relaxation time, k_B is the Boltzmann constant, and e is the charge of an electron. Note that in ensemble averaging of momentum relaxation time, we use the Boltzmann distribution function instead of the Fermi-Dirac distribution. The Fermi energy of electrons in each MoS_2 layer is given by

$$\varepsilon_F = k_B T \ln\left(e^{-\frac{\pi\hbar^2 n}{g_v m^* k_B T}} - 1\right), \qquad \text{(S3)}$$

where n is the 2D electron density and g_v=6 is the valley degeneracy. Due to the high electron effective mass m^*~m_0 where m_0 is the bare electron mass, and the high valley degeneracy, MoS_2 behaves as a non-degenerate semiconductor. For example, for a carrier density n=5×10^{13}/cm^2, the Fermi energy lies 4 meV (<<k_BT=25 meV @ 300K) above the conduction band edge at room temperature.

Scattering mechanisms considered to model the experimental data are: i) ionized impurity scattering, ii) acoustic phonon scattering, and ii) optical phonon scattering. For ionized impurity scattering, the impurities are assumed to be at the two surfaces of each MoS_2 layer (similar to the ionized impurity scattering in graphene[34]) as shown in Supplementary Fig. S7(a). The energy-dependent momentum relaxation time is calculated using Fermi's Golden rule.

For screening by free carriers, a finite-temperature Thomas-Fermi screening model is used. The finite-temperature Thomas-Fermi wave vector is given by

$$q_{TF}(T) = \frac{2g_v}{a_B^*}\left(1 - e^{-\frac{\pi\hbar^2 n}{g_v m^* k_B T}}\right), \tag{S4}$$

where a_B^* is the bulk Bohr radius in MoS_2.

Acoustic phonons are low energy excitations of coherent lattice vibrations with energy dispersion of $E(q)=\hbar v_\lambda q$, where v_λ is the phonon velocity (sound velocity) of phonon mode λ, and q is the wave vector of phonons. As a result, the electron-acoustic phonon scattering can be considered as an elastic scattering mechanism. Under deformation potential approximation, the acoustic phonon limited mobility can be written as

$$\mu_{ac}(T)=\frac{e\hbar^3\sigma_s v_\lambda^2}{\left(m^*\right)^2\Xi_\lambda^2 k_B T}, \tag{S5}$$

where σ_s =6.4 x10^{-6} kg/m^2 is the areal mass density of multilayer MoS$_2$, and Ξ_λ is the acoustic deformation potential. In the calculation of electron-acoustic phonon scattering, a nondegenerate ($E(q) << k_B T$) phonon spectrum is assumed. The justification lies on the fact that the characteristic Bloch Grüneisen (BG) temperature $T_{BG}=\sqrt{\frac{4\pi n}{3}}\left(\frac{v_\lambda}{k_B}\right)$ above which the phonon spectrum is nondegenerate, is low even at high carrier densities. For example, for $n=10^{13}$/cm^3, the BG temperature of multilayer MoS$_2$ is $T_{BG}\approx$32 K. The reason for of the low BG temperature is the high valley degeneracy in multilayer MoS$_2$ film. Using this impurity density and fitting the measured carrier mobility over the temperature range, we extract acoustic deformation potentials $\Xi_{LA}\approx$ 2.6 eV for LA phonons and $\Xi_{TA}\approx$ 1 eV for TA phonons respectively. Though the extraction of deformation potentials from a single transport measurement involves a certain level of uncertainty, nevertheless these values are similar to the deformation potentials values of single layer MoS$_2$ predicted recently[35] using density functional calculations. This is justified since the in-plane transport properties of multilayer MoS$_2$ should resemble that of a single layer due to the weak van der Waals interaction between adjacent layers. Future atomistic simulations and transport experiments are expected to reveal the more accurate values of these parameters of multilayer MoS$_2$ and determine the relative importance of different scattering mechanisms at room temperature.

For optical phonon scattering, two types of optical phonons are considered: a) polar optical phonon mode, and b) homopolar optical phonon mode. In polar optical phonon mode, the two sulfur atoms in a MoS$_2$ unit cell move in the same direction whereas the metal atom moves in the opposite direction as shown in Supplementary Fig S7(c). This mode has an energy

$\hbar\omega_{\mathrm{op}}$=0.049 eV at the Γ point of the Brillioun zone[36]. The high polar optical phonon energy inhibits emission and only phonon absorption occurs in electron-optical phonon scattering events at low electric fields (in the mobility-regime). For electron-polar optical phonon scattering, we use the results of Gelmont and Shur[37] originally developed for 2D electron gas transport in GaN high-electron mobility transistors.

For the homopolar optical phonon mode, the two sulfur atoms move in opposite directions as shown in Supplementary Fig. S6(b). The net dipole moment associated with this mode vanishes due to the inversion symmetry about the metal plane resulting a non-polar optical phonon mode. The homopolar phonon limited mobility in MoS_2 is given by[38]

$$\mu_{hp}(T) = \frac{e}{8\pi m^* \omega_{hp} g^2} \frac{\left(e^{\frac{\hbar\omega_{hp}}{k_B T}} - 1\right)}{1 + \frac{\hbar\omega_{hp}}{2k_B T}}, \qquad \text{(S6)}$$

where g ($\sim\varepsilon_d^2$, ε_d is the deformation potential) is a dimensionless coupling constant and $\hbar\omega_{\mathrm{hp}}$ is the homopolar optical phonon energy. The value of g is extracted by fitting the transport data with the theory. A reasonable fit in Fig. 4(a) of the main text is found for g=0.08. This leads to a deformation potential $\varepsilon_d \approx$ 3 eV, comparable to the previously reported[38] value of 6 eV. The above transport theory is based on the assumption that the applied electric field is small. The small electric field is implicitly defined by the relation $v_d << v_{th}$, where $v_d = e\tau E/m^*$ (E = applied electric field) is the drift velocity of carriers due to applied electric field and v_{th} is the mean thermal velocity. For a Maxwellian velocity distribution of carriers in 2D $f(v)=(m^*/2\pi k_B T)\exp[-m^* v^2/(2k_B T)]$, and the mean thermal velocity is $v_{th}=(\pi k_B T/2m^*)^{1/2}$. This leads to a critical electric field $E_{cr}=(1/e\tau)(\pi m^* k_B T/2)^{1/2}$, below which the low-field theory is valid. For mobility $\mu \sim$ 100 cm^2/V·s ($\tau \sim 5\times10^{-15}$ s), the critical field is $E_{cr} \approx 10^5$ V/cm. As the mobility values were extracted from the linear (ohmic) region of the I_D-V_{ds} curve (see Fig. 2(d)), the applied electric field is $E=(V_{ds}\ -2I_D R_c)/L$ in contrast to the saturation region. For I_D~5μA, V_{ds}~ 1V and L=4 μm, the typical applied field is $E\sim 10^3$ V/cm, which is orders of magnitude lower than the critical field E_{cr}. This justifies the linear response modeling.

Supplementary Tables

Material	Bandgap (eV)	Dielectric constant	Conduction band degeneracy	Electron effective mass	Heavy Hole eff. mass	Dopant act. ener. (meV)	Intrinsic Conc. n_i (cm^{-3})
MoS_2	1.3	4.3	6	1.0	1.0	6	1.6×10^{8}
Si	1.12	11.9	6	0.33	0.49	10	1.0×10^{10}
Al_2O_3	6.5	7.0					

Supplementary Table S1: Material properties of silicon, ALD Al_2O_3, and multilayer MoS_2 used for the energy band-diagram calculations. Note that the anisotropic properties of MoS_2 are included through requisite averaging.

Supplementary References

[28] Y. Taur and T. H. Ning, *Fundamentals of Modern VLSI Devices*, 2nd Ed., Cambridge University Press, p85-94.

[29] C. Nassar et al., Single Fermi Level Thin-Film CMOS on Glass: The Behavior of Enhancement-Mode PMOSFETs From Cutoff Through Accumulation, *IEEE Trans. Electron Dev.*, **56** (9) 1974-1979 (2009).

[30] 1D Poisson, available online from http://www.nd.edu/~gsnider.

[31] B. L. Evans, "Optical Properties of Layer Compounds", in Optical and Electrical Properties, vol, 4 of Physics and Chemistry of Materials with Layered Structures, Reidel (1976).

[32] W. Monch, Valence-band offsets and Schottky barrier heights of layered semiconductors explained by interface-induced gap states, *Appl. Phys. Lett.*, **72** 1899-1901 (1998).

[33] Seeger, K. *Semiconductor Physics: An Introduction*, 7th Ed., Springer-Verlag, New York, 1999.

[34] Hwang, E. H., Adam, S. and Sarma, S. D., Carrier Transport in Two-Dimensional Graphene Layers, *Phys. Rev. Lett.*, **98**, 186806-186810 (2007).

[35] Kaasbjerg, K., Thygesen, K. S., and Jacobsen, K. W., Phonon-limited mobility in n-type single-layer MoS_2 from first principles, *Phys. Rev. B* **85**, 115317 (2012).

[36] Bromley, R., The Lattice Vibrations of MoS_2 Structures, *Philos. Mag.*, **28**, 1417-1427 (1971).

[37] Gelmont, B. L. and Shur, M., Polar optical-phonon scattering in three- and two-dimensional electron gases, *J. Appl. Phys.*, **77**, 657-660 (1995).

[38] Fivaz, R. and Mooser, E., Electron-Phonon Interactions in Semiconducting Layer Structures, *Phys. Rev.*, **136**, A833-A836 (1964).